Regular Article

Self-assembly of defined core–shell ellipsoidal particles at liquid interfaces

Jack Eatson [a,1], Susann Bauernfeind [b,c,1], Benjamin Midtvedt [d], Antonio Ciarlo [d], Johannes Menath [c], Giuseppe Pesce [d,e], Andrew B. Schofield [b], Giovanni Volpe [d], Paul S. Clegg [b], Nicolas Vogel [c], D. Martin. A. Buzza [a], Marcel Rey [b,d,f,*]

[a] Department of Physics and Astrophysics, G. W. Gray Centre for Advanced Materials, University of Hull, Hull HU6 7RX, United Kingdom
[b] School of Physics and Astronomy, The University of Edinburgh, Peter Guthrie Tait Road, Edinburgh EH9 3FD, UK
[c] Institute of Particle Technology (LFG), Friedrich-Alexander-Universität Erlangen-Nürnberg (FAU), Cauerstrasse 4, 91058 Erlangen, Germany
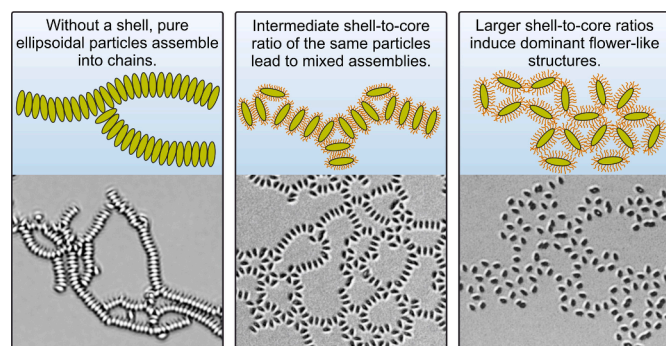[d] Department of Physics, University of Gothenburg, SE-41296 Gothenburg, Sweden
[e] Dipartimento di Fisica "Ettore Pancini", Università degli Studi di Napoli Federico II, Naples, Italy
[f] University of Münster, Institute of Physical Chemistry, Corrensstr. 28/30, 48149 Münster, Germany

GRAPHICAL ABSTRACT

ARTICLE INFO

ABSTRACT

Hypothesis: Ellipsoidal particles confined at liquid interfaces exhibit complex self-assembly due to quadrupolar capillary interactions, favouring either tip-to-tip or side-to-side configurations. However, predicting and controlling which structure forms remains challenging. We hypothesize that introducing a polymer-based soft shell around the particles will modulate these capillary interactions, providing a means to tune the preferred self-assembly configuration based on particle geometry and shell properties.

Experiments: We fabricate core–shell ellipsoidal particles with defined aspect ratios and shell thickness through thermo-mechanical stretching. Using interfacial self-assembly experiments, we systematically explore how aspect ratio and shell thickness affect the self-assembly configurations. Monte Carlo simulations and theoretical calculations complement the experiments by mapping the phase diagram of thermodynamically preferred structures as a function of core–shell properties.

* Corresponding author at: School of Physics and Astronomy, The University of Edinburgh, Peter Guthrie Tait Road, Edinburgh EH9 3FD, UK.
  E-mail address: mrey@uni-muenster.de (M. Rey).
  [1] These authors contributed equally.

Findings: Pure ellipsoidal particles without a shell consistently form side-to-side "chain-like" assemblies, regardless of aspect ratio. In contrast, core–shell ellipsoidal particles exhibit a transition from tip-to-tip "flower-like" arrangements to side-to-side structures as aspect ratio increases. The critical aspect ratio for this transition shifts with increasing shell thickness. Our results highlight how we can engineer the self-assembly of anisotropic particles at liquid interfaces by tuning their physicochemical properties such as aspect ratio and shell thickness, allowing the deterministic realization of distinct structural configurations.

1. Introduction

When particles adsorb to a liquid interface, they reduce the direct contact between the two phases, lower the overall free energy of the system [1], and provide mechanical strength to the interface due to jamming [2,3]. This can lead to the formation of stable foams [4–7], emulsions [8–13], bijels [14,15] or liquid marbles [16,17], with a wide range of applications, including in the food industry [8,9], cosmetics [18], and medical fields [19–22]. Furthermore, the interfacial assembly can be transferred onto solid substrates to obtain nanoscale surface patterns with high fidelity over macroscopic areas [23]. These patterns are exploited in photonic [24] and phononic [25] applications, and serve as a template for the fabrication of more complex plasmonic nanostructure [26,27] and nanowire arrays [28,29].

Liquid interfaces further confine colloidal particles to two dimensions, enabling the study and control of their self-assembly behaviour. Monodispersed spherical colloidal particles typically self-assemble into hexagonal structures, influenced by the balance of attractive capillary and van-der-Waals forces and repulsive electrostatic and dipole forces [30,31]. For rough or nonspherical particles, strong lateral capillary interactions arise due to interface deformation caused by an undulating contact line or particle shape effects [32–37]. These dominant capillary interactions between the particles not only enhance the stability of foams [38] or emulsions [39–41], possibly through strong effects on the interfacial rheology [39], but also dictate their self-assembly behaviour at liquid interfaces [34,37,42].

For ellipsoidal particles at liquid interfaces, the deformation of the meniscus along the long axis differs from that along the short axis, resulting in capillary forces with quadrupolar symmetry that greatly exceed the thermal energy $k_{B}T$ [34]. The saddle-like distortion field around the ellipses causes them to attract each other either tip-to-tip or side-to-side, while repelling each other in the side-to-tip configuration [33,34,37].

Both tip-to-tip and side-to-side configurations have been found experimentally. At the oil/water interface, sterically-stabilized ellipsoidal particles self-assembled into a side-to-side configuration, corroborated by calculations and simulations as the energetically most stable configuration [43,44]. Selectively removing the steric stabilizer from the tip of the ellipsoidal particles changed the self-assembly into tip-to-tip configurations [45]. The self-assembly behaviour of charge-stabilized ellipsoidal particles is less understood. At an air/water interface, side-to-side [46–49] and tip-to-tip [34,46,49,50] arrangements have been reported. In one study, ellipsoidal particles with low aspect ratios assembled preferentially side-to-side, while a tip-to-tip arrangement was found for higher aspect ratios [46]. Another study reported "flower-like" tip-to-tip arrangements at the air/water interface, whereas the same particles formed a "chain-like" tip-to-tip arrangement at a decane/water interface [50]. This difference was rationalized by the different contact angle of the ellipsoidal particles adsorbed at the air/water and decane/water interface, respectively [50]. Additionally, core–shell ellipsoidal particles consisting of an incompressible core and a hydrogel shell initially self-assembled into a side-to-side assembly, which transitioned over time into a tip-to-tip assembly [51]. Furthermore, the shell thickness of these core–shell ellipsoidal particles was reported to affect their assembly, with thicker shells resulting in a tip-to-tip arrangement, while thinner shells led to a side-to-side assembly [52]. Interestingly, similar assembly pattern have been observed in natural

systems, such as Anopheline mosquito eggs floating on water [53]. Depending on their subspecies, these eggs characteristically assemble into either side-to-side or tip-to-tip structures. To summarize, both tip-to-tip and side-to-side arrangements for seemingly similar ellipsoidal particles have been observed experimentally. However, the origin of the preference for either structure is not yet fully understood and deterministic control of their self-assembly thus remains challenging.

A convenient and frequently used method to produce ellipsoidal particles with controlled aspect ratios is the thermo-mechanical stretching technique [54,55]. However, we recently discovered that in this fabrication process, the cleaning protocol significantly impacts the behaviour of ellipsoidal particles due to residual polymer chains that remain on their surfaces [56]. These polymer residues impact the behaviour of both the individual particle and the particle dispersion. Contrary to the previous belief that the anisotropic shape of ellipsoidal particles prevents the coffee ring effect [57], our findings demonstrated that it is actually the presence of polymeric residues adsorbed on the particle surface that leads to homogeneous drying [56]. When these polymer residues are properly removed using an appropriate solvent [47], the ellipsoidal particles exhibit the coffee ring effect [56]. We therefore hypothesize that the potential presence of polymer residues, an artifact of the fabrication, or cleaning process, may similarly affect the interfacial self-assembly and thus explain the variety of different assembly structures reported for ellipsoidal particles.

Here, we experimentally and computationally investigate the interfacial self-assembly behaviour of core–shell ellipsoidal particles, focussing on the role of the shell provided by water-soluble polymer chains adsorbed to the particle surface. By carefully controlling the fabrication process and cleaning protocol, we synthesize either pure ellipsoidal particles or core–shell ellipsoidal particles with polymeric hairs on their surfaces. These polymers significantly influence the self-assembly of the ellipsoidal particles. Pure ellipsoidal particles consistently assemble into a side-to-side arrangement, independent of their aspect ratio. In contrast, core–shell ellipsoidal particles exhibit a transition from a tip-to-tip assembly at lower aspect ratios to a side-to-side assembly at higher aspect ratios, with the onset of this transition shifting to higher aspect ratios as the relative shell size (i.e., the ratio of shell to core) increases. We support our experimental observations with theoretical calculations and Monte Carlo simulations, mapping out the phase diagram for core–shell ellipsoidal particles as a function of aspect ratio and shell thickness, which accurately reproduces the experimental results.

2. Materials and methods

2.1. Materials

All chemicals were obtained from commercial sources and used as received if not otherwise stated. Acrylic acid (99 %, Sigma Aldrich), ammonium persulfate (APS, 98 %, Sigma Aldrich), azobisisobutyronitrile (>97 %, VWR), Polyvinylpyrrolidone PVP K90 (PVP, 360′000 k$_D$, Sigma Aldrich), methyl methacrylate (>99 %, Sigma Aldrich), methanol (99.8 %, Sigma Aldrich), polyvinyl alcohol (PVA, Mw 146.000–186.000, 87–89 % hydrolyzed, Sigma Aldrich), ethanol (99.9 %, Sigma Aldrich) and glycerol (99.5 %, Sigma Aldrich) were used as received.

Double-filtered and deionized water (18.2 MΩ·cm, double reverse osmosis by Purelab Flex 2, ELGA Veolia) was used throughout this study. Styrene as monomer (ReagentPlus with 4-*tert*-butyl catechol as a

stabilizer, $\geq$99 %, Sigma Aldrich) was washed with 10 wt-% NaOH aqueous solution to remove the inhibitor. The monomer was subsequently purified by flash column chromatography with activated Al_2O_3 (basic 90 for column chromatography, Carl Roth) using nitrogen gas.

2.2. Polystyrene (PS) particle synthesis

PS particles with a radius of 0.55 μm were synthesized using a surfactant-free emulsion polymerization method. In a 500 mL triple-neck round-bottom flask, 250 mL of water was heated to 80 °C and degassed by bubbling nitrogen gas for 30 min. Then, 80 g of styrene and 0.4 g of the comonomer acrylic acid, dissolved in 5 mL of water, were added under constant stirring. After 5 min, 0.1 g of APS, dissolved in 5 mL of water, was introduced. The reaction was carried out at 80 °C for one day. Following this, the mixture was cooled to room temperature, filtered, and purified through a series of centrifugation, redispersion, and dialysis against water for two months.

We note that acrylic acid was solely added to provide additional negative charge to the particle surface, allowing us to synthesize them with diameters exceeding 1 μm. Although acrylic acid may influence interactions with PVP and PVA, our previous work demonstrated that the surface chemistry of the particles has surprisingly little effect on the adsorption behaviour of PVA and PVP [56]. Significant adsorption was observed across all types of surface modifications [56].

For the synthesis of smaller PS particles with a radius of 0.19 μm (used to measure the polymer shell thickness and zeta potential via dynamic light scattering (Malvern Zetasizer Nano ZS, Fig. S1), a similar protocol was followed with adjusted reactant concentrations. Specifically, 10 g of styrene, 0.1 g of acrylic acid, and 0.1 g of APS were used.

2.3. Polymethyl methacrylate (PMMA) particle synthesis

PMMA particles with a radius of 1.65 μm were synthesized using a dispersion polymerisation method. In a one litre bottle, 45 g of PVP K90 (360'000 k_D) is dissolved in 400 g of methanol. The fluorescent comonomer 7-nitrobenzo-2-oxa-1,3-diazole-methyl methacrylate was prepared according to the instructions of Jardine and Bartlett [58]. 0.375 g of this comonomer was dissolved in 15 g of methanol. Once these ingredients were fully dissolved, they were transferred to a one litre three-necked round-bottomed flask. Into this flask was also added 27.5 g of methyl methacrylate and 46 g of distilled water. The necks of the flask were fitted with a stirrer, a nitrogen inlet and a condenser. The flask was placed in an oil bath and the reaction mixture brought to reflux (72 °C). Whilst adjusting this flask to reflux, 0.375 g of the initiator azobisisobutyronitrile was dissolved in 10 g of methyl methacrylate. Once reflux had been achieved, the initiator system was added and the reaction allowed to proceed for 24 h. After this time the reaction mixture was allowed to cool to room temperature and the particles were cleaned by centrifugation and redispersion in excess methanol six times. For the seventh step, the centrifugation was repeated and then the particles were dispersed in the minimum amount of methanol possible and then excess water was added to the dispersion. A further three centrifugation and redispersion steps were completed except this time distilled water was used as the suspending fluid. The particles were kept in distilled water prior to use.

2.4. Ellipsoidal particle fabrication

Ellipsoidal particles were prepared using the established method by Ho et al. [55]. For pure ellipsoidal particles (without any adsorbed polymers) and PVA-coated ellipsoidal particles, 6.75 g of PVA is dissolved in 100 mL of distilled water heated to 90 °C under continuous stirring. After the PVA dissolves, the solution is cooled to room temperature, and 5 mL of a 2 wt% PS particle dispersion is added. For PVP-coated particles, 10 g of PVP is dissolved in 100 mL of distilled water at 90 °C under stirring. After cooling, 1.1 g of glycerol is added to improve

the ductility of the matrix. Then, 2 mL of a 13 wt% PMMA dispersion or 8 mL of a 2 wt% PS particle dispersion is added. Both the PVA and PVP particle mixtures are spread into thin films on lacquered aluminium plates in a fume hood and dried for 24 h.

The dried films were cut into 2×8 cm^2 strips and fixed into a custom-made stretching device. The PVP films were additionally heated in an oven at 60 °C to ensure complete evaporation of any entrapped water. A household fryer equipped with a stirrer was used as an oil bath. For PVA matrices, the oil bath was set to 135 °C, while for PVP matrices, it was set to 160 °C. The fixed film was placed in the oil bath for five seconds, followed by variable stretching depending on the desired ellipsoid aspect ratios. The film was then cooled to room temperature and cleaned with a tissue soaked in isopropanol (IPA) to remove any remaining oil.

The middle part of the stretched film (approximately 5 cm) was cut out and dissolved in water. If not stated otherwise, the PVA and PVP-coated ellipsoidal particles were all cleaned four times by centrifugation and redispersion in water. Pure ellipsoidal particles were obtained by cleaning the ellipsoidal particles stretched in PVA matrices an additional three times with a 3:7 IPA/water mixture, followed by three times with water using centrifugation and redispersion. The same procedure was used for PVP-coated ellipsoidal particles in Fig. 1f. The arithmetic mean long and short axes of the ellipsoidal particles were determined by measuring 100 particles in SEM images (GeminiSEM 500, Carl Zeiss AG, Germany).

## 2.5. Interfacial self-assembly and optical microscopy imaging

The experiments were performed using video microscopy (CCD camera, IDS UI-3060CP-M−GL R2) using a custom-built inverted optical microscope. We obtained different magnifications by using either a 20× or a 40× Nikon air immersion objective. Two glass slides (Marienfeld, size 1.5), in one of them was a 5 mm circular hole cut, were glued together to create a sample cell. The cell was filled with 5 μL of water. The aqueous ellipsoidal particle dispersion was mixed with 15 vol% ethanol as spreading agent and 0.1 μL of the dispersion was spread at the liquid interface. To avoid potential issues and misinterpretations due to jamming and interface crowing, we resort to a dilute regime where the available interfacial area is much larger than the number of particles under investigation. For each sample, at least 10 images were taken.

2.6. Surface evolver

The capillary interaction energy and the amplitude of contact line undulations were calculated using Surface Evolver, a finite element method which represents the interface as a mesh of triangles and displaces vertices to minimize energy subject to constraints [59]. An adjustable triangular mesh between $0.02b − 0.1b$ with quadratic edge lengths was used to capture the shape of the interface near the contact line more accurately. Since the interactions between the ellipsoidal particles are essentially quadrupolar and fall off rapidly with separation, a relatively small simulation box with reflecting boundary conditions at $x = \pm 6a$ and $y = \pm 6a$ was used. To calculate the capillary interaction potential between two ellipsoidal particles, the reflecting walls to calculate the interfacial energy of a single ellipsoidal particle interacting with its image at a reflecting wall was exploited, varying the particle surface-to-reflecting wall distance from $0.1b$ to $3a$ and using the ellipsoidal particle at the centre of the simulation box to represent the 'infinite' separation case.

2.7. Monte Carlo (MC) simulations

Using a customised code, NVT Metropolis simulations on an ensemble of 625 core–shell ellipsoidal particles with periodic boundary conditions were performed using a fixed rectangular box with aspect
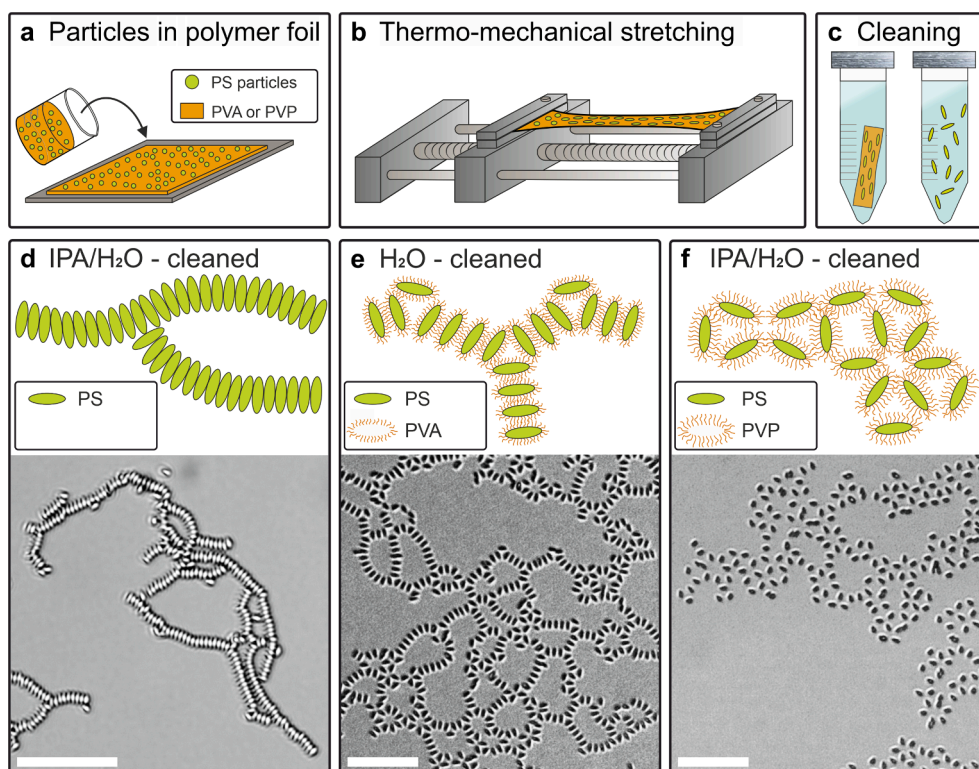
Fig. 1. The self-assembly behaviour of ellipsoidal particles at the air/water interface depends on their fabrication process. (a–c) Schematic illustration of the fabrication process: (a) Colloidal polystyrene (PS, radius $R_0 = 0.55$ µm) particles are embedded in a PVA or PVP film, followed by (b) thermo-mechanical stretching. (c) The ellipsoidal particles are recovered by dissolving the film in H_2O followed by cleaning using centrifugation and redispersion in either pure H_2O or IPA/H_2O mixtures. (d–f) Schematic illustration and optical microscopy images of the interfacial self-assembly at an air/water interface for ellipsoidal particles prepared by different fabrication procedures. (d) Ellipsoidal particles prepared in a PVA film and cleaned in an IPA/H_2O mixture assemble in direct contact in a "chain-like" side-to-side arrangement. (e) The same ellipsoidal particles but cleaned solely with H_2O assemble in a mixture of side-to-side and tip-to-tip configurations and retain a non-close packed arrangement. (f) Ellipsoidal particles prepared in a PVP film assemble in a "flower-like" tip-to-tip configuration with non-close packed arrangement, even when cleaned with an IPA/H_2O mixture. Scale bars: 20 µm.

ratio $2:\sqrt{3}$ with particles initially arranged in a hexagonal array with random azimuthal orientations. We define the threshold concentration for the dilute regime to be the core area fraction $\eta_c = \pi ab/4(a+h)^2$, i.e., the highest core area fraction where core–shell ellipsoidal particles on a square lattice can freely rotate about their centres without interfering with each other. In our simulations, we use a core area fraction $\eta = \eta_c/2$ to ensure that the system is in the dilute regime. Each MC move consisted of a simultaneous translation and rotation move, with an adjustable maximum translational distance of d_{max} and azimuthal rotation angle of d_{max}/a about the particle centre to ensure an acceptance probability of 30 % for the MC moves. The particles were initially randomized at a high temperature of $T^* = 100$ for 10^3 attempted moves per particle, then quenched to $T^* = 0.2$ for a further 10^6 attempted moves per particle. To confirm that our simulations are long enough to effectively equilibrate the system, we have performed longer simulations with 2×10^6 attempted moves per particle and found that the longer simulations resulted in statistically similar final structures to the shorter simulations for all the cases we studied. To reduce computation time, particle interactions for separations greater than a cutoff distance of $2a + 10b$ were neglected.

2.8. Particle detection and measurements

The positions and orientations of the particles were determined using a deep learning approach [60,61]. First, a U-Net predicted the distance transform map of the segmentation of each particle, normalized per particle such that the maximum value of the distance transform map is 1. The distance transform map was preferred as a target over immediately

predicting the segmentation map since it better distinguished closely packed particles.

Once the distance transform map is acquired, instance segmentations of the particles were determined. Two binary segmentations were calculated by comparing the distance transform map to two simple thresholding criteria, the values of which were determined using a hyperparameter sweep on a holdout set after training. The first, sparser binarization was used to detect the individual particles. The second binarization was used as a panoptic foreground segmentation of the image. Finally, the watershed algorithm was applied to the two binarizations to acquire instance segmentation maps.

Next, orientation and the minor and major axes of the particles were estimated using the Python library *scipy* applied to the individual instance segmentations. The minor and major axes were additionally used as a sanity check, lightly filtering detections that are too far outside the range of expected sizes.

2.9. Neural network data annotation and training

To efficiently collect sufficient annotated data for training the artificial neural network (ANN), an active learning approach was used. First, each experimental image was split into 128×128 pixel^2 patches with a 50 % overlap. Initially, a uniformly sampled selection of 20 such patches was presented to an oracle to annotate using an ad-hoc user interface by drawing ellipses over the particles in view.

From this, an initial training dataset was constructed using the Python libraries *Deeplay* and *DeepTrack* [60,61]. First, since the samples are monodisperse, we normalized the sizes of all annotated ellipses to the median ellipse for each experiment. The target image was computed

as the normalized distance transformation map of each ellipse. In the case of overlapping ellipses, the maximum value of the overlapping ellipses' distance transform map for each conflicting pixel was used. During training, the images were augmented using integer multiples of $90°$ rotations, random horizontal mirroring, and a high pass filter with a random cutoff frequency.

Using this initial dataset, a committee of five ANNs was trained for 20 epochs each, using L_1 loss, a batch size of 32, and an Adam optimizer with a learning rate of 0.001. This committee was subsequently used to query the most valuable patches for further annotations by the oracle. First, the prediction of each ANN on each image was computed. Second, the patch was sampled using the following scheme: (i) a particle type was randomly chosen to ensure a diverse sampling; (ii) for each patch not yet annotated, the disagreement within the committee as the average pixel-wise variance was calculated; (iii) one patch at random from the top 10 % scoring patches was selected to alleviate overfitting the criterion.

The scheme was repeated until a desired budget was exhausted. The budget was set to 100 patches. A validation set was created in parallel, where each patch was sampled uniformly from all not yet annotated patches for a given experiment. This ensured that the validation results were not biased by the training data sampling criterion.

For each selected patch, the oracle was presented by the ellipses acquired by the process described by the method outlined in the previous section. The user tuned this prediction by deleting false positive ellipses and adding missed ellipses. This increased annotation significantly since most patches had only a few errors. The annotated data was added to the training pool, and a new committee was trained. This process was repeated until desired F1-score was reached on the validation-set. Once sufficient data had been annotated for the desired quality, a final ANN was trained using the same training parameters as the committee, but for a total of 100 epochs.

2.10. Statistical analysis of clusters

Particles were classified as belonging to side-to-side chains or tip-to-tip triangular clusters based on their separation and orientation relative to other particles in the system, with the criteria based on these quantities chosen to ensure that the classification coincides with the classification based on visual inspection. For this analysis, the centre-to-centre separation between two nearest-neighbour core–shell ellipsoidal particles in contact was $d_C = 2b'$ and $d_T = \sqrt{a'^2 + 3b'^2}$ respectively for the side-to-side chains and tip-to-tip triangular lattices shown in Fig. 5d [62], where $a' = a + h$, $b' = b + h$. For the simulation system, a particle was classified as belonging to a side-to-side chain if its centre-to-centre separation to any other particle satisfied the condition $r_{12} < 1.3d_C$ and the relative orientation of the two particles satisfied the condition $|\hat{a}_1 \cdot \hat{a}_2| \geq 0.9$, where $\hat{a}_1$, $\hat{a}_1$ are the unit vectors along the semi-major axes of the two particles. On the other hand, a particle as belonging was classified to a tip-to-tip triangular cluster if its centre-to-centre separation to any other particle satisfied $0.7d_T \leq r_{12} \leq 1.15d_T$ and the relative orientation of the two particles satisfied $|\hat{a}_1 \cdot \hat{a}_2| < 0.9$. If a particle belonged to both a chain and a triangular cluster, we classified it as belonging to a triangular cluster. The statistical classification above was carried out for a single snapshot (containing 625 particles) for each aspect ratio and shell thickness.

For the experimental system, a neural network was used to analyse the experimental micrographs to capture the position of the ellipsoidal particle centres, the long and short axes lengths and the orientation of the long axis relative to one of the lab frame axes. The data was then filtered by eliminating any particles whose long axis length is smaller than 60 % of the mean or two standard deviations greater than the mean. Further, any overlapping particles were removed by assuming that all ellipsoidal particles have a long and short axes length equal to the mean and all particle pairs whose centre-to-centre separation is smaller than

the contact separation predicted by the Berne-Pechukas model [63] were also removed from the analysis (see Supplementary Information). We note that the neural network underpredicts the aspect ratio of the ellipsoidal particles compared to values obtained from direct measurements of the experimental micrographs but fortunately this discrepancy does not have a significant impact on our statistical classification. Having filtered the experimental data as described above to remove any artefacts of the ellipsoidal particle identification process, an ellipsoidal particle was classified as being part of a side-to-side chain if its separation and orientation relative to any other particle satisfied the conditions $r_{12} < 1.3d_C$, $|\hat{a}_1 \cdot \hat{a}_2| \geq 0.9$ and $|\hat{a}_1 \cdot \hat{r}_{12}| < 0.5$, where $\hat{r}_{12}$ unit vector along the centre-to-centre line connecting the two particles. On the other hand, an ellipsoidal particle was classified as being part of a tip-to-tip triangular cluster if its separation and orientation relative to any other particle satisfied the conditions $0.5d_T \leq r_{12} \leq 0.8d_T$, $|\hat{a}_1 \cdot \hat{a}_2| < 0.9$ and $|\hat{a}_1 \cdot \hat{r}_{12}| > 0.2$. If an ellipsoidal particle belonged to both a chain and a triangular cluster, we classified it as belonging to a triangular cluster. The statistical classification above was carried out for $4 - 20$ experimental micrographs (containing 3200–37,000 particles) for each aspect ratio and shell thickness.

3. Results and discussion

3.1. The interfacial self-assembly behaviour of ellipsoidal particles is influenced by their fabrication and cleaning procedures

We compare the self-assembly of polymeric polystyrene (PS) ellipsoidal particles with an aspect ratio (AR) of about 3 at the air/water interface, produced using the thermo-mechanical stretching technique [55] with different fabrication protocols. In the fabrication process, spherical PS colloidal particles (radius $R_0 = 0.55$ μm) are embedded in either a poly(vinyl alcohol) (PVA) or poly(vinyl pyrrolidone) (PVP) films (Fig. 1a) [54]. This composite film is stretched in an oil bath above the glass transition temperature of the polymeric particles, deforming them into ellipsoidal particles (Fig. 1b). The resulting anisotropic particles are subsequently retrieved by dissolving the films in water, followed by cleaning in either an isopropanol (IPA)/water mixture or pure water (Fig. 1c).

The synthesized ellipsoidal particles are then spread at an air/water interface using ethanol as spreading agent, and their self-assembly in the dilute regime under conditions of low interfacial coverage is observed in situ using optical microscopy. A striking difference is observed depending on the fabrication protocol. Ellipsoidal particles prepared following the original work by Ho et al. [55] using a PVA film and cleaning in IPA/water mixtures, self-assemble into a "chain-like" structure, where the ellipsoidal particles are in direct contact in a side-to-side configuration (Fig. 1d). The same ellipsoidal particles but cleaned using dissolution and subsequent centrifugation/redispersion in water, self-assemble into a non-close-packed structure where the ellipses are visibly separated from each other. They assume both side-to-side and tip-to-tip configurations (Fig. 1e). Ellipsoidal particles prepared in a PVP film, on the other hand, assemble into a "flower-like" tip-to-tip configuration (Fig. 1f), but also visibly separated and non-close-packed.

We attribute the difference in self-assembly behaviour to the presence of polymeric chains adsorbed onto the particle surface during the fabrication process. An IPA/water mixture is required to sufficiently remove PVA from the ellipsoidal particle surfaces [55,56]. In contrast, using pure water for the cleaning process by centrifugation/redispersion cycles leaves a layer of PVA chains on the particle surface with a thickness in swollen state of roughly 40 nm (Fig. S1a) and a decrease in zeta potential by approximately an order of magnitude (Fig. S1b), as determined by dynamical light scattering [56]. Analytical ultracentrifugation further revealed a PVA volume fraction of 4.9 %, corresponding to a PVA surface coverage of 2.3 mg m^{-2} [56]. These PVA chains extend at the liquid interface to reduce the surface energy and thereby form a

2D corona around the ellipsoidal particles, which is even visible in situ using cryo-scanning electron microscopy (SEM) [47]. This polymer shell prevents the particles from coming into close contact and, as we will discuss later, affects the energy landscape of the tip-to-tip and side-to-side configurations. We note that the ellipsoidal particles coated with PVP (Fig. 1f) are visibly more separated compared to the ones coated with PVA (Fig. 1e), despite both polymers having a comparable contour length. We speculate that intra-polymer hydrogen bonds in PVA [64] may hinder the spreading of the polymers along the liquid interface, leading to a smaller shell area of PVA compared to PVP.

Assembling PVA-coated ellipsoidal particles at liquid interfaces is challenging. Typically, particles are spread at the liquid interface using ethanol or isopropanol as spreading agents. However, when these spreading agents are mixed with the particle dispersion, PVA is readily removed from the particle surface, making it difficult to control their behaviour at liquid interfaces. To overcome this challenge, we replaced the PVA matrix used in the stretching process with PVP (poly-vinylpyrrolidone). PVP polymer chains remain at least partially attached to the ellipsoidal particle surface even after cleaning with an IPA/water mixture (Fig. 1f, Fig. S1). These ellipsoidal particles thus retain their polymer shell after spreading at the air/water interface, evidenced by the non-close-packed arrangement at the liquid interface (Fig. 1f) and thus allow a systematic and reliable study of their self-assembly as a function of aspect ratio and shell-to-core ratio. Therefore, from this point forward, core–shell ellipsoidal particles with a PVP shell are used in this manuscript.

In bulk liquid, both PVA (166 kDa) and PVP (360 kDa) chains produce a similar shell thickness of around 40 nm (Fig. S1a). However, ellipsoidal particles with a PVP shell appear more separated at the air/water interface compared to those with a PVA shell (cf. Fig. 1e, f). We hypothesize that PVP chains extend further at the liquid interface, leading to a more extended corona around the ellipsoidal particles than PVA chains. Although the exact mechanism is not yet fully understood, our data suggest that the physicochemical properties of the polymer shell significantly influence corona formation at liquid interfaces, which, in turn, affects the self-assembly behaviour of the ellipsoidal particles.

3.2. The interfacial self-assembly behaviour of core–shell ellipsoidal particles is influenced by their aspect ratio and shell-to-core ratio

We next investigate how the self-assembly behaviour of these ellipsoidal particles varies with aspect ratio (Fig. 2). Spherical polymethyl methacrylate (PMMA) particles (radius $R_0 = 1.65$ μm) coated with PVP remain fully separated (Fig. 2a), indicating predominant repulsive interactions. In contrast, when stretched into ellipsoidal particles, they exhibit attractive interactions at the liquid interface (Fig. 2b–h). At low aspect ratios, ellipsoidal particles primarily form a "flower-like" tip-to-tip assembly (Fig. 2b–d). As the aspect ratio increases, "flower-like" and "chain-like" structures with side-to-side arrangement coexist (Fig. 2d–f). These ellipsoidal particles form network-like structures where tip-to-tip triangles form branching points of individual side-by-side chains. The length of the chains continuously increases, until, at the highest aspect ratios (AR > 6), the predominant assembly is in the form of chains.

Next, we quantify the interfacial self-assembly behaviour of the ellipsoidal particles as a function of their shell-to-core ratio and aspect ratio (Fig. 3, Fig. 4). Experimentally, we vary the shell-to-core ratio, h/R_0, by stretching colloidal particles with different initial radii ($R_0 = 0.55$ μm and $R_0 = 1.65$ μm), while maintaining the same PVP shell polymer (Fig. 3a–j, Fig. S2). The interfacial shell thickness h formed by the PVP polymer chains stretched at the liquid interface is quantitatively determined by averaging over the distances between ellipsoidal particles in the side-to-side configuration (Fig. S3). This model assumes that the ellipsoidal particles in this configuration are in shell contact, which seems reasonable as capillary forces will tend to bring the particles into the closest possible configuration. The measurements in Fig. S3 confirm that h/R_0 remains independent of the aspect ratio. It is important to note that the PVP shell thickness in bulk is roughly 40 nm, but once adsorbed to the liquid interface, the PVP polymer chains can extend to form a micron-sized 2D shell, also termed a corona, along the interface as they spread out to reduce surface tension [56,65]. We note that the ellipsoids appear larger and rounder in the optical microscopy images (Fig. 3) compared to electron microscopy images (Fig. S2) due to the limited resolution of the optical microscopy as our particles are close to the diffraction limit.

To quantify the self-assembled structures at the interface, we employ a U-Net deep-learning model combined with the watershed algorithm to
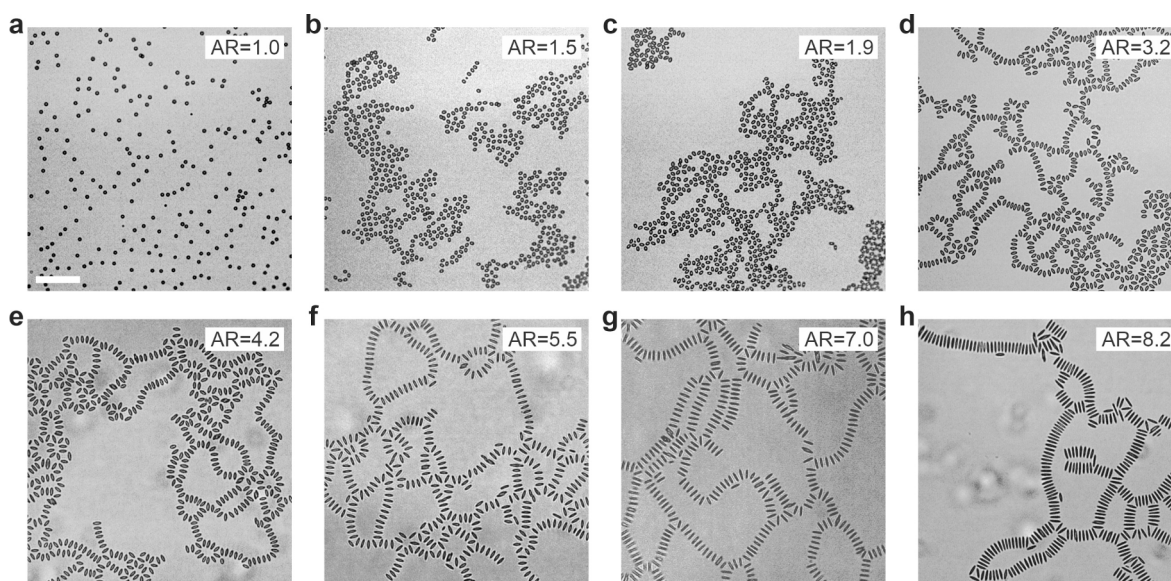
Fig. 2. Interfacial self-assembly behaviour of PMMA-PVP core–shell ellipsoidal particles as a function of aspect ratio (AR). Microscopy images of the self-assembly of (a) spherical particles and (b–h) ellipsoidal particles with increasing aspect ratio (AR). We observe a transition from a "flower-like" tip-to-tip assembly (b–d) to a "chain-like" side-to-side assembly (e–h). Scale bar: 50 μm.
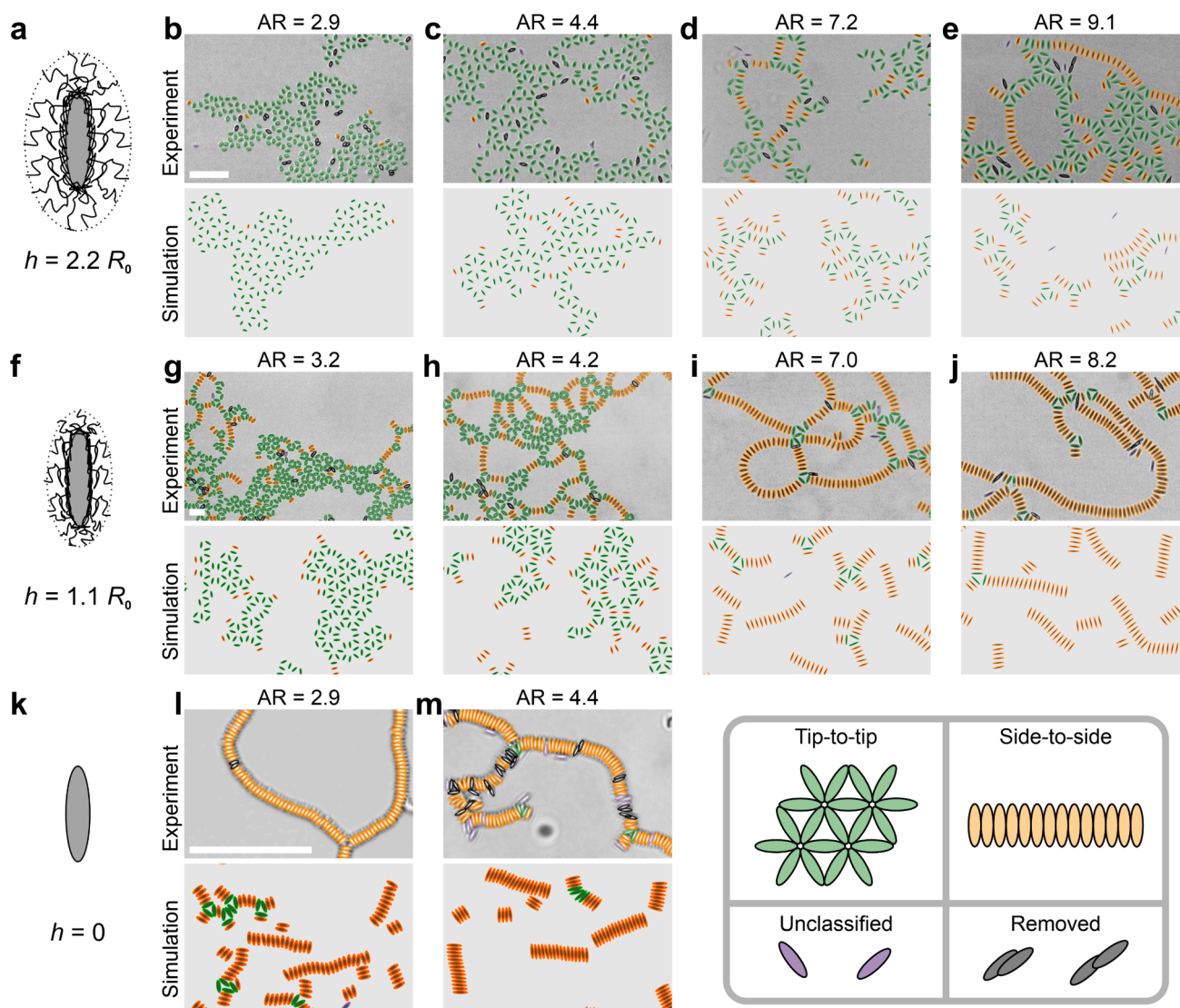
Fig. 3. Self-assembly of core–shell ellipsoidal particles at the air/water interface as a function of shell thickness *h* and aspect ratio AR. (a,f,k) Schematic illustration of the core–shell ellipsoidal particles. (b-e, g-j,l-m) Microscopy images (top) with colour-coded overlay and corresponding Monte Carlo simulations (bottom). Ellipsoidal particles in tip-to-tip are colour-coded green, in side-to-side orange, unclassified purple and ill-defined, removed ellipsoidal particles in black. (a–e) PS-PVP ellipsoidal particles with a shell thickness $h = 2.2\,R_0$ predominantly assemble in tip-to-tip configuration at low and intermediate aspect ratios (b,c) and coexistence of tip-to-tip and side-to-side at higher aspect ratio (d,e). (f–j) PMMA-PVP ellipsoidal particles with a shell thickness $h = 1.1\,R_0$ assemble in a tip-to-tip configuration at low aspect ratio (g), a mixture of tip-to-tip and side-to-side at intermediate aspect ratio (h) and side-to-side at high aspect ratio (i,j). (k–m) Ellipsoidal PS particles without a shell ($h = 0$) only assemble side-to-side. Scale bars: 20 μm. (For interpretation of the references to color in this figure legend, the reader is referred to the web version of this article.)

obtain instance-level segmentations of the particles [60,61]. These segmentations are used to extract the position, size, and orientation of the particles through ellipse fitting. We then classify the particle configurations as either tip-to-tip (green), side-to-side (orange) or unclassified (purple) by comparing the distance and orientation of each ellipse to its nearest neighbours. Ill-defined particles (black) are excluded from the analysis. The color-coded outlines of the ellipses are then overlayed onto the microscopy images (Fig. 3, top rows). A detailed description of the segmentation and categorization protocol is provided in the Methods section.

We find that ellipsoidal particles with the higher shell-to-core ratio (Fig. 3a–e, $h = 2.2\,R_0$), produced using polystyrene particles with an initial radius $R_0 = 0.55$ μm, predominantly assemble in a "flower-like" tip-to-tip structure at low and intermediate aspect ratios (Fig. 3b,c). At higher aspect ratios, there is a notable coexistence with a "chain-like" side-to-side structure (Fig. 3d,e). A similar pattern is observed for ellipsoidal particles with a lower shell-to-core ratio (Fig. 3f–j, $h = 1.1$

R_0), where tip-to-tip structures are present at low aspect ratios (Fig. 3g), coexistence is seen at intermediate aspect ratios (Fig. 3h), and side-to-side configurations dominate at higher aspect ratios (Fig. 3i, j). However, the transition to side-to-side configurations occurs at lower aspect ratios for these ellipsoidal particles. Ellipsoidal particles without a shell (Fig. 3k-m, $h = 0$) were fabricated via removing a PVA shell in an IPA/water mixture similar to Fig. 1d. Experimentally, we find essentially only "chain-like" side-to-side assemblies (Fig. 3l,m), irrespective of aspect ratio. These trends are quantitatively confirmed through a statistical analysis of the structures formed, as shown in Fig. 4.

3.3. Monte Carlo simulations corroborate the experimental self-assembly behaviour

To gain a deeper understanding of the fundamental forces driving the self-assembly of core–shell ellipsoidal particles at the liquid interface, we perform Monte Carlo (MC) simulations of core–shell ellipsoidal
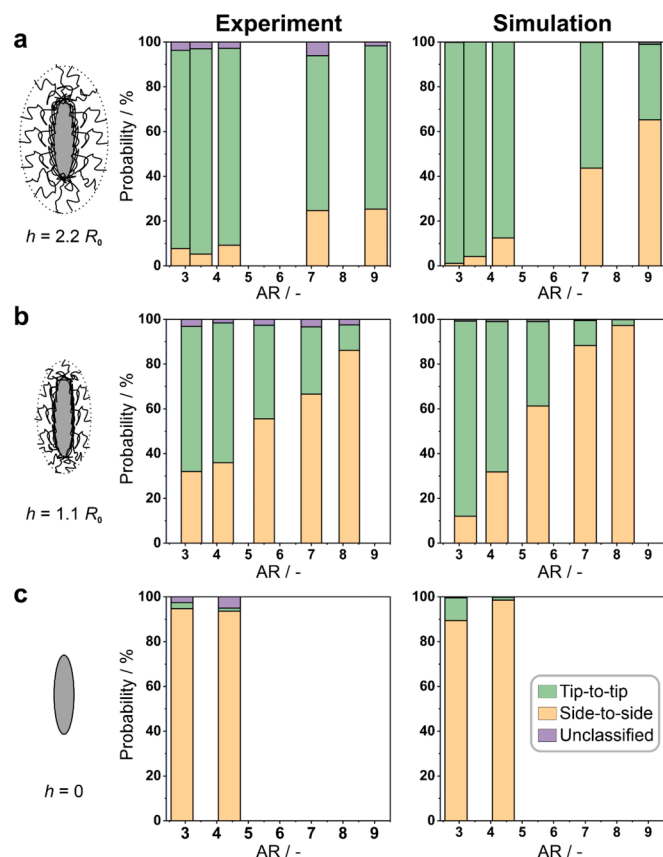
Fig. 4. Quantitative analysis of the self-assembly behaviour of core–shell ellipsoidal particles. Probability of finding ellipsoidal particles in a tip-to-tip (green) or side-to-side (orange) configuration. For core–shell ellipsoidal particles (a,b), there is a continuous transition from a tip-to-tip assembly to a side-to-side assembly with increasing aspect ratio. (c) Ellipsoidal particles without a shell almost exclusively assemble into side-to-side configurations. (For interpretation of the references to color in this figure legend, the reader is referred to the web version of this article.)

particles with aspect ratios and shell thicknesses h corresponding to the experimental system, including both steric and capillary interactions between the particles. For simplicity, we neglect electrostatic repulsions as steric stabilization appears to be the dominant mechanism governing particle stability.

As discussed earlier, the PVP chains adsorbed to the ellipsoidal particle core are stretched out more significantly at the liquid interface compared to the bulk. The steric interactions between the core–shell ellipsoidal particles are therefore primarily due to the more extended 2D shell formed by the interfacial PVP chains rather than the 3D shell formed by the bulk PVP chains. In Refs. [65,66], we studied the self-assembly of core–shell particles at liquid interfaces that were subjected to an external compression where it is sometimes energetically favourable for the shells of neighbouring particles to locally collapse so that their cores come into contact. In contrast, the core–shell particles we are studying here are not subjected to any external compression and the steric repulsion between the 2D shells is sufficient to prevent particles from coming closer than shell-shell contact, as experimentally evidenced by the formed non-close-packed patterns (Fig. 1, Fig. 2). In the experiments, we also observe that this shell repulsion occurs at both the sides and the tips of particles and, for simplicity, we assume that the shell thickness is the same at the sides and the tips. In our MC simulation, we therefore treat the core–shell ellipsoidal particles as hard ellipses with long and short axis lengths of $a' = a + h$ and $b' = b + h$ respectively, where h is the experimentally measured shell thickness which is independent of the aspect ratio AR (Fig. S3). From the conservation of the

core volume, the long and short axis lengths of the core are given by $a = R_0 AR^{2/3}$, $b = R_0 AR^{-1/3}$ respectively. Specifically, we reject any MC move that causes particles to come closer than the contact separation between the hard ellipses σ_c, where σ_c is calculated using the Berne-Pechukas model [63], see Supplementary Information. Note that since the cores are separated on the micron-scale by the 2D shell in the experimental system, short range interactions between the cores such as hydrogen bonds or van der Waals interactions (with ranges on the nanometer-scale) can be safely neglected in our simulations.

The capillary interactions between the core–shell ellipsoidal particles come from the quadrupolar deformation of the three-phase contact line on the ellipsoidal particle surface due to the constant contact angle requirement at the contact line [37]. Note that the contact line resides on the PVP-coated core rather than the boundary of the shell, as we assume that the shell is essentially a 2D object formed by interfacially adsorbed polymer chains. In addition, it is reasonable to assume that the PVP shell renders the core more hydrophilic and we therefore assign a water contact angle of the core as $\theta_w = 40^\circ$ in our model [47]. To model the capillary interactions between the core–shell ellipsoidal particles, we treat each ellipsoidal core as a capillary quadrupole in elliptical coordinates [35,67] and the resultant expression for the capillary interaction potential is given in Supplementary Information. The advantage of working in elliptical coordinates is that it allows us to accurately model the capillary interactions between rod-like particles using a small number of capillary multipoles [35], in our case one multipole at quadrupolar order. To verify the accuracy of the model, we compare the model (solid lines) to Surface Evolver simulations (data points) for the capillary interaction energy V as a function of the inter-particle separation r_{12} in Fig. 5a and Fig. S5. We compare ellipsoidal particles with no shells in the side-to-side configuration (orange) and tip-to-tip configuration (green) for lower aspect ratio ellipsoidal particles where the numerical simulations are stable. Note that in these figures, we have used H_e, the amplitude of the elliptical quadrupole, as a fitting parameter to fit the model to the Surface Evolver data. The fitted values of H_e for different aspect ratio AR are given in Table S1. The model captures the key features of the numerical data almost quantitatively, including the far-field quadrupolar scaling of $V \sim -1/r_{12}^4$ (dashed black line) and the near-field deviations from this scaling, confirming that modelling the contact line undulations as elliptical quadrupoles is a good approximation. In particular, the model correctly predicts that the lowest energy configuration for two ellipsoidal particles with no shells is a side-to-side contact rather than tip-to-tip contact (note that we plot $-V$ in the vertical axis of Fig. 5a and Fig. S5).

The MC simulations were performed at a core area fraction of $\eta = \pi ab/8a'^2$ to ensure that the system is in the dilute regime (i.e., core–shell ellipsoidal particles can initially freely rotate about their centres without interfering with each other, see Methods and Materials section) like in the experiments. The energy scale for capillary interactions is γH_e^2, where γ is the interfacial tension of the air–water interface (see Supplementary Information). The importance of capillary interactions relative to the thermal energy is therefore characterized by the normalized temperature $T^* = k_B T/\gamma H_e^2$ and in Table S1 in Supplementary Information, we show that the experimental system is effectively in the low temperature regime $T^* \ll 1$. To model the experimental system, we therefore quench the system from a high initial temperature to a final temperature of $T^* = 0.2$. The choice of the final temperature represents a good compromise between being low enough for the system to be in the low temperature regime and still being high enough for the MC simulation to equilibrate the system efficiently. Further details of the MC and Surface Evolver simulations can be found in Methods.

In Fig. 3, we show final snapshots from the MC simulations of core–shell particles for different aspect ratios and shell thicknesses (bottom rows) and directly compare them to their experimental counterparts (top rows). The MC simulation accurately reproduces the experimentally observed trends, namely that increasing aspect ratio favours the
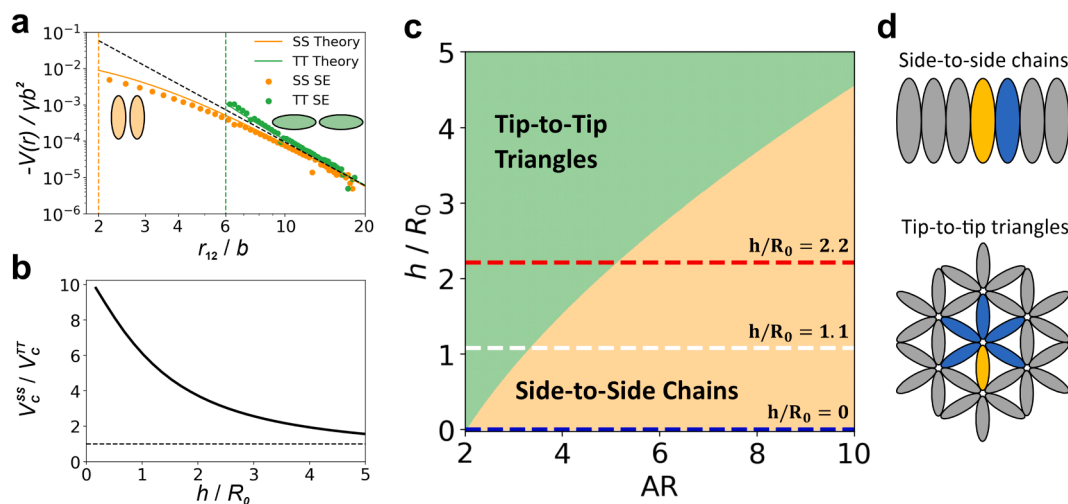
Fig. 5. Theoretical evaluation of interactions between core–shell ellipsoidal particles at liquid interfaces. (a) Capillary interaction energy between two bare ellipsoidal particles (i.e., no shell) with aspect ratio 3 as a function of centre-to-centre separation r_{12} normalized by the length of the short axis of the ellipsoidal particles, b, for ellipsoidal particles oriented side-to-side (orange) and tip-to-tip (green). The lines are calculated analytically assuming the ellipsoidal particles are elliptical quadrupoles while the points are calculated numerically using Surface Evolver. Note that we are plotting $-V$ on the vertical axis. The orange and green dashed vertical lines denote the centre-to-centre separation for side-to-side and tip-to-tip contact respectively while the black dashed line represents the quadrupolar power law. (b) Ratio of capillary energies for core–shell ellipsoidal particles in side-to-side vs. tip-to-tip contact as a function of shell thickness h calculated from analytical theory assuming the cores are elliptical quadrupoles. Note that this ratio is always greater than unity (horizontal black dashed line) for all h values studied. (c) Zero temperature phase diagram for core–shell ellipsoidal particles in the aspect ratio (AR) vs. shell to core ratio h/R_0 plane. The experimental values of h/R_0 are indicated by the blue, white and red dashed lines, respectively. (d) Minimum energy configurations of side-to-side chains and tip-to-tip triangular lattice that are used to compute the phase diagram, where the energy per particle is calculated from the interaction between the yellow particle and its neighbouring blue particles. (For interpretation of the references to color in this figure legend, the reader is referred to the web version of this article.)

formation of "chain-like" side-to-side arrangements, while increasing shell thickness favours "flower-like" tip-to-tip configurations. We quantitatively analyse the MC simulation snapshot using the same statistical analysis as for the experimental data (see Methods for further details). In Fig. 4, we quantitatively compare the statistical classification of the different structures formed in the MC simulations as a function of the aspect ratio and shell thicknesses with their experimental counterparts. The data confirms that the MC simulation reproduces the experimentally observed trend that increasing aspect ratio favours the formation of "chain-like" side-to-side arrangements, while increasing shell thickness favours "flower-like" tip-to-tip formations.

We note from the snapshots in Fig. 3 that for each aspect ratio and shell thickness, the MC simulations not only reproduce the proportion of side-to-side chains versus tip-to-tip triangular lattices but also the local microstructure of the particle clusters and networks that are observed experimentally. One feature of the microstructure that is not captured so well by the simulations is that the cluster size of side-to-side chains tend to be smaller than what is observed experimentally, especially for the higher aspect ratio ellipsoidal particles. We attribute this discrepancy to two reasons. First, the interaction potential for side-to-side contacts is lower than for tip-to-tip contacts and this energy difference increases with increasing aspect ratio so that the relaxation time for side-to-side chains is much longer compared to tip-to-tip triangular lattices in the low temperature regime for larger aspect ratio ellipsoidal particles. Second, the area fraction we use in the simulations roughly scales as AR^{-1} and therefore decreases with increasing aspect ratio AR. These factors mean that for the same overall simulation length, the higher aspect ratio systems are not as well equilibrated as the lower aspect ratio systems, resulting in smaller side-to-side chain lengths and cluster sizes for higher aspect ratio systems. However, apart from this discrepancy, the agreement between simulation and experiments for both the statistics and the local microstructure of the self-assembled structures is remarkable, especially considering the minimalistic assumptions of our theoretical model. The fact that our simulations capture the key features of the experiments suggests that the self-assembly of core–shell ellipsoidal particles is primarily driven by a competition between steric

repulsions from the shell and capillary interactions from the core, while electrostatic interactions seem to play a negligible role.

3.4. Minimum energy calculations rationalize the transition between tip-to-tip and side-to-side arrangement

To assess the thermodynamics underpinning the observed self-assembled structures, we first consider how the interaction potential between core–shell ellipsoidal particles varies with aspect ratio and shell thickness. As we increase the aspect ratio of the core–shell ellipsoidal particles, side-to-side contacts become increasingly more energetically favourable compared to tip-to-tip contacts, essentially because the difference in centre-to-centre separation between the two configurations increases, see Fig. S5 in SI. This explains why increasing aspect ratio favours the formation of side-to-side chains compared to tip-to-tip triangular lattices.

In Fig. 5a, we focus on the role of shell thickness on the assembly process, using ellipsoidal particles with an aspect ratio of 3 as a model. We first note that as we increase the shell thickness h, the fractional increase in the centre-to-centre separation r_{12} will be greater for ellipsoidal particles in side-to-side contact compared to those in tip-to-tip contact. Since from Fig. 5a, the capillary interaction between the ellipsoidal cores is to a first approximation an inverse power law in r_{12} (black dashed line), this means that the capillary bond energy (i.e., the magnitude of the attractive potential at contact) for core–shell ellipsoidal particles in side-to-side contact should drop more than those in tip-to-tip contact as we increase shell thickness. This point is confirmed in Fig. 5b where we plot the ratio V_c^{SS}/V_c^{TT} as a function of shell thickness h for core–shell ellipsoidal particles with aspect ratio AR $= 3$, where V_c^{SS} and V_c^{TT} are the capillary bond energies for side-to-side and tip-to-tip contacts respectively calculated from the elliptical quadrupole model. We see that the capillary bond energy for side-to-side contacts falls relative to that for tip-to-tip contacts as we increase h. Despite this decrease, we note that $V_c^{SS}/V_c^{TT} > 1$ for the shell thicknesses explored in this study, i.e., the capillary bond energy for side-to-side contact is

always greater than that for tip-to-tip contact, so that this effect alone is not enough to tip the balance in favour of the formation of tip-to-tip structures.

However, in both the experiments and the simulations, the core–shell ellipsoidal particles with large h do not form tip-to-tip chains but "flower-like" tip-to-tip triangular lattices, where the number of capillary bonds per particle is greater than in the chain state. Specifically, the number of capillary bonds per particle is 1 for side-to-side chains and 5 for tip-to-tip triangular lattices, as schematically shown in Fig. 5d by the interactions between a central particle (yellow) and its neighbours (blue). In Fig. 5c, we quantify the total capillary interactions for side-to-side and tip-to-tip arrangements as a function of aspect ratio and shell thickness, taking into account both the evolution of V_c^{SS}/V_c^{TT} with shell thickness, and the increased number of neighbours for triangular tip-to-tip lattices. These calculations are based on the elliptical quadrupole model [35,67] (see Supplementary Information), where the centre-to-centre separation between nearest neighbours in shell-to-shell contact is calculated using the analytic formula given in Ref. [62].

In our calculations, we assume the structures are infinite, i.e., we neglect defects and edge effects. We also neglect interactions of the yellow particle with particles beyond the blue particles, i.e., we assume an effective cutoff distance of $\approx a' = a + h$ for particle interactions; this is a good approximation since we are considering quadrupolar interactions which fall off rapidly with separation. Finally, we assume that the equilibrium structure for any given geometry is the structure with the minimum energy per particle. This assumption is justified since the experimental system is in the low temperature regime $T^* \ll 1$ where entropic effects are negligible. Fig. 5c shows the resultant zero-temperature phase diagram for core–shell ellipsoidal particles in the aspect ratio AR-shell thickness h plane.

This phase diagram accurately reproduces the trends observed in both experiments and simulations. Increasing the aspect ratio favours the formation of side-to-side chains, while increasing shell thickness favours the formation of tip-to-tip triangular lattices. In particular, it predicts that as we increase shell thickness from $h/R_0 = 0$ via $h/R_0 = 1.1$ to $h/R_0 = 2.2$ (blue, white and red horizontal lines, respectively), the transition from tip-to-tip triangular lattices to side-to-side chains occurs at higher and higher aspect ratios. Note that we do not see pure phases but a coexistence of different phases in both the experiments and the simulations, indicating that the system is not globally ergodic. However, the fact that the equilibrium structures predicted by the zero-temperature phase diagram correlate well with the dominant structures seen in both experiments and simulations suggests that the structures shown in Fig. 5d are kinetically accessible and the experimental core–shell ellipsoidal particle system is at least locally ergodic.

4. Conclusions

This study investigates the self-assembly of polymer-coated ellipsoidal particles fabricated through thermo-mechanical stretching at liquid interfaces, emphasizing the significant role of soft polymer shells formed during fabrication. At a liquid interface, these polymer shells, which spread under the influence of surface tension, create a two-dimensional barrier that prevents direct contact between neighbouring ellipsoidal particles and alters the minimum energy landscape. As a result, pure ellipsoidal particles consistently form side-to-side "chain-like" assemblies, regardless of aspect ratio, while core–shell ellipsoidal particles demonstrate a transition from tip-to-tip "flower-like" configurations to side-to-side arrangements as the aspect ratio increases. This transition is influenced by the interplay between shell thickness and aspect ratio, highlighting the critical importance of shell properties in determining self-assembly behaviour.

Our findings also reconcile previously conflicting reports in the literature [34,46–50] regarding the self-assembly of ellipsoidal particles at the air/water interface, where the self-assembly of seemingly similar

particles has been reported as both side-to-side [46–49] and tip-to-tip [34,46,49,50] arrangements. Notably, our previous work has demonstrated that the thermo-mechanical stretching process leaves behind a polymer coating on the stretched particles, which can only be removed through a suitable cleaning protocol [56]. We interpret that these earlier studies likely involved particles that also had polymer shells, without considering their influence in the interpretation. As a result, the particles may have been treated as hard, rigid entities, overlooking the significant influence of the soft polymer coating. This study highlights the significance of these polymer shells in influencing interfacial interactions and self-assembly behaviour, thereby advancing our understanding of how to manipulate particle configurations at liquid interfaces.

The introduction of a phase diagram mapping preferred structures based on core and shell properties provides a robust framework for designing anisotropic particles with tailored assembly behaviours. Future research could explore interfacial compression of the polymeric shells, potentially revealing predicted phase transitions [68] analogous to those observed in spherical core–shell systems [65]. Expanding this framework to accommodate other particle geometries and dimensions will further generalize the principles of programmable self-assembly at liquid interfaces [42]. Additionally, incorporating stimuli-responsive polymer shells—sensitive to temperature [10], pH [65], or light [69]—could enable reconfigurable assemblies, adding dynamic functionality to these assemblies. The framework presented in this study is general and offers a foundation for the predictive design of anisotropic core–shell particles that self-assemble into predetermined, complex arrangements, opening new pathways for engineering advanced self-assembling structures.

Declaration of competing interest

The authors declare that they have no known competing financial interests or personal relationships that could have appeared to influence the work reported in this paper.

Acknowledgements

Appendix A. Supplementary data

Supplementary data to this article can be found online at https://doi.org/10.1016/j.jcis.2024.12.156.

Data availability

Data will be made available on request.

References

[1] P. Pieranski, Two-dimensional interfacial colloidal crystals, Phys. Rev. Lett. 45 (1980) 569–572, https://doi.org/10.1103/PhysRevLett.45.569.

[2] V. Garbin, Collapse mechanisms and extreme deformation of particle-laden interfaces, Curr. Opin. Colloid Interface Sci. 39 (2019) 202–211, https://doi.org/10.1016/j.cocis.2019.02.007.

[3] E.L. Correia, N. Brown, S. Razavi, Janus particles at fluid interfaces: stability and interfacial rheology, Nanomaterials 11 (2021) 1–29, https://doi.org/10.3390/nano11020374.

[4] B.P. Binks, T.S. Horozov, Aqueous foams stabilized solely by silica nanoparticles, Angew. Chem. – Int. Ed. 44 (2005) 3722–3725, https://doi.org/10.1002/anie.200462470.

[5] E. Dickinson, Food emulsions and foams: stabilization by particles, Curr. Opin. Colloid Interface Sci. 15 (2010) 40–49, https://doi.org/10.1016/j.cocis.2009.11.001.

[6] S. Lam, K.P. Velikov, O.D. Velev, Pickering stabilization of foams and emulsions with particles of biological origin, Curr. Opin. Colloid Interface Sci. 19 (2014) 490–500, https://doi.org/10.1016/j.cocis.2014.07.003.

[7] N. Brown, A. de la Pena, S. Razavi, Interfacial rheology insights: particle texture and Pickering foam stability, J. Phys. Condens. Matter 35 (2023) 384002, https://doi.org/10.1088/1361-648X/acde2c.

[8] N. Nimaming, A. Sadeghpour, B.S. Murray, A. Sarkar, Pickering oil-in-water emulsions stabilized by hybrid plant protein-flavonoid conjugate particles, Food Hydrocoll. 154 (2024) 110146, https://doi.org/10.1016/j.foodhyd.2024.110146.

[9] E. Tenorio-Garcia, A. Araiza-Calahorra, M. Rappolt, E. Simone, A. Sarkar, Pickering water-in-oil emulsions stabilized solely by fat crystals, Adv. Mater. Interfaces 10 (2023) 2300190, https://doi.org/10.1002/admi.202300190.

[10] M. Rey, J. Kolker, J.A. Richards, I. Malhotra, T.S. Glen, N.Y.D. Li, F.H.J. Laidlaw, D. Renggli, J. Vermant, A.B. Schofield, S. Fujii, H. Löwen, P.S. Clegg, Interactions between interfaces dictate stimuli-responsive emulsion behaviour, Nat. Commun. 14 (2023) 6723, https://doi.org/10.1038/s41467-023-42379-z.

[11] S.J. Stubley, O.J. Cayre, B.S. Murray, I.C. Torres, Emulsifying properties of sugar beet pectin microgels, Food Hydrocoll. 137 (2023) 108291, https://doi.org/10.1016/j.foodhyd.2022.108291.

[12] M.F. Haase, D. Grigoriev, H. Moehwald, B. Tiersch, D.G. Shchukin, Encapsulation of amphoteric substances in a pH-sensitive Pickering emulsion, J. Phys. Chem. C 114 (2010) 17304–17310, https://doi.org/10.1021/jp104052s.

[13] T.G. Anjali, M.G. Basavaraj, General destabilization mechanism of pH-responsive Pickering emulsions, PCCP 19 (2017) 30790–30797, https://doi.org/10.1039/c7cp04665k.

[14] E.M. Herzig, K.A. White, A.B. Schofield, W.C.K. Poon, P.S. Clegg, Bicontinuous emulsions stabilized solely by colloidal particles, Nat. Mater. 6 (2007) 966–971, https://doi.org/10.1038/nmat2055.

[15] D.J. French, A.B. Schofield, J.H.J. Thijssen, Bicontinuous soft solids with a gradient in channel size, Adv. Mater. Interfaces 9 (2022), https://doi.org/10.1002/admi.202102307.

[16] S. Fujii, S.I. Yusa, Y. Nakamura, Stimuli-responsive liquid marbles: controlling structure, shape, stability, and motion, Adv. Funct. Mater. 26 (2016) 7206–7223, https://doi.org/10.1002/adfm.201603223.

[17] R. Murakami, H. Moriyama, M. Yamamoto, B.P. Binks, A. Rocher, Particle stabilization of oil-in-water-in-air materials: powdered emulsions, Adv. Mater. 24 (2012) 767–771, https://doi.org/10.1002/adma.201104089.

[18] S. Yue, W. Shen, K. Hapgood, Characterisation of liquid marbles in commercial cosmetic products, Adv. Powder Technol. 27 (2016) 33–41, https://doi.org/10.1016/j.apt.2015.10.014.

[19] N.M. Oliveira, R.L. Reis, J.F. Mano, The potential of liquid marbles for biomedical applications: a critical review, Adv. Healthc. Mater. 6 (2017) 1–15, https://doi.org/10.1002/adhm.201700192.

[20] T. Arbatan, L. Li, J. Tian, W. Shen, Liquid marbles as micro-bioreactors for rapid blood typing, Adv. Healthc. Mater. 1 (2012) 80–83, https://doi.org/10.1002/adhm.201100016.

[21] C.L.G. Harman, M.A. Patel, S. Guldin, G.L. Davies, Recent developments in Pickering emulsions for biomedical applications, Curr. Opin. Colloid Interface Sci. 39 (2019) 173–189, https://doi.org/10.1016/j.cocis.2019.01.017.

[22] A. Jamburidze, A. Huerre, D. Baresch, V. Poulichet, V. De Corato, V. Garbin, Nanoparticle-coated microbubbles for combined ultrasound imaging and drug delivery, Langmuir 35 (2019) 10087–10096, https://doi.org/10.1021/acs.langmuir.8b04008.

[23] V. Lotito, T. Zambelli, Approaches to self-assembly of colloidal monolayers: a guide for nanotechnologists, Adv. Colloid Interface Sci. 246 (2017) 217–274, https://doi.org/10.1016/j.cis.2017.04.003.

[24] M. Kolle, P.M. Salgard-Cunha, M.R.J. Scherer, F. Huang, P. Vukusic, S. Mahajan, J.J. Baumberg, U. Steiner, Mimicking the colourful wing scale structure of the Papilio blumei butterfly, Nat. Nano 5 (2010) 511–515, https://doi.org/10.1038/nnano.2010.101.

[25] N. Boechler, J.K. Eliason, A. Kumar, A.A. Maznev, K.A. Nelson, N. Fang, Interaction of a contact resonance of microspheres with surface acoustic waves, Phys. Rev. Lett. 111 (2013) 1–5, https://doi.org/10.1103/PhysRevLett.111.036103.

[26] T. Honold, K. Volk, A. Rauh, J.P.S. Fitzgerald, M. Karg, Tunable plasmonic surfaces via colloid assembly, J. Mater. Chem. C Mater. 3 (2015) 11449–11457, https://doi.org/10.1039/x0xx00000x.

[27] A. Nemiroski, M. Gonidec, J.M. Fox, P. Jean-Remy, E. Turnage, G.M. Whitesides, Engineering shadows to fabricate optical metasurfaces, ACS Nano 8 (2014) 11061–11070, https://doi.org/10.1021/nn504214b.

[28] M. Rey, F.J. Wendisch, E.S. Aaron Goerlitzer, J.S. Julia Tang, R.S. Bader, G.R. Bourret, N. Vogel, Anisotropic silicon nanowire arrays fabricated by colloidal lithography, Nanoscale Adv. 3 (2021) 3634–3642, https://doi.org/10.1039/d1na00259g.

[29] F.J. Wendisch, M.S. Saller, A. Eadie, A. Reyer, M. Musso, M. Rey, N. Vogel, O. Diwald, G.R. Bourret, Three-dimensional electrochemical axial lithography on Si micro- and nanowire arrays, Nano Lett. 18 (2018) 7343–7349, https://doi.org/10.1021/acs.nanolett.8b03608.

[30] N. Vogel, M. Retsch, C.A. Fustin, A. Del Campo, U. Jonas, Advances in colloidal assembly: the design of structure and hierarchy in two and three dimensions, Chem. Rev. 115 (2015) 6265–6311, https://doi.org/10.1021/cr400081d.

[31] R. Aveyard, J.H. Clint, D. Nees, V.N. Paunov, Compression and structure of monolayers of charged latex particles at air / water and octane / water interfaces, Langmuir 16 (2000) 1969–1979, https://doi.org/10.1021/la990887g.

[32] D. Stamou, C. Duschl, D. Johannsmann, Long-range attraction between colloidal spheres at the air-water interface: the consequence of an irregular meniscus, Phys. Rev. E Stat. Phys. Plasmas Fluids Relat. Interdiscip. Top. 62 (2000) 5263–5272, https://doi.org/10.1103/PhysRevE.62.5263.

[33] J.C. Loudet, A.G. Yodh, B. Pouligny, Wetting and contact lines of micrometer-sized ellipsoids, Phys. Rev. Lett. 97 (2006) 1–4, https://doi.org/10.1103/PhysRevLett.97.018304.

[34] J.C. Loudet, A.M. Alsayed, J. Zhang, A.G. Yodh, Capillary interactions between anisotropic colloidal particles, Phys. Rev. Lett. 94 (2005) 2–5, https://doi.org/10.1103/PhysRevLett.94.018301.

[35] H. Lehle, E. Noruzifar, M. Oettel, Ellipsoidal particles at fluid interfaces, Euro. Phys. J. E 26 (2008) 151–160, https://doi.org/10.1140/epje/i2007-10314-1.

[36] T.G. Anjali, M.G. Basavaraj, Shape-anisotropic colloids at interfaces, Langmuir 35 (2019) 3–20, https://doi.org/10.1021/acs.langmuir.8b01139.

[37] L. Botto, E.P. Lewandowski, M. Cavallaro, K.J. Stebe, Capillary interactions between anisotropic particles, Soft Matter 8 (2012) 9957–9971, https://doi.org/10.1039/c2sm25929j.

[38] P.J. Beltramo, M. Gupta, A. Alicke, I. Liascukiene, D.Z. Gunes, C.N. Baroud, J. Vermant, Arresting dissolution by interfacial rheology design, PNAS 114 (2017) 10373–10378, https://doi.org/10.1073/pnas.1705181114.

[39] B. Madivala, S. Vandebril, J. Fransaer, J. Vermant, Exploiting particle shape in solid stabilized emulsions, Soft Matter 5 (2009) 1717–1727, https://doi.org/10.1039/b816680c.

[40] H. Kumar, V.R. Dugyala, M.G. Basavaraj, Phase inversion of ellipsoid-stabilized emulsions, Langmuir 37 (2021) 7295–7304, https://doi.org/10.1021/acs.langmuir.1c00456.

[41] V.R. Dugyala, T.G. Anjali, S. Upendar, E. Mani, M.G. Basavaraj, Nano ellipsoids at the fluid-fluid interface: effect of surface charge on adsorption, buckling and emulsification, Faraday Discuss. 186 (2016) 419–434, https://doi.org/10.1039/c5fd00136f.

[42] J.L. Eatson, S.O. Morgan, T.S. Horozov, D.M.A. Buzza, Programmable 2D materials through shape-controlled capillary forces, Proc. Natl. Acad. Sci. 121 (2024) e2401134121, https://doi.org/10.1073/pnas.2401134121.

[43] A.M. Luo, J. Vermant, P. Ilg, Z. Zhang, L.M.C. Sagis, Self-assembly of ellipsoidal particles at fluid-fluid interfaces with an empirical pair potential, J. Colloid Interface Sci. 534 (2019) 205–214, https://doi.org/10.1016/j.jcis.2018.08.114.

[44] L. Botto, L. Yao, R.L. Leheny, K.J. Stebe, Capillary bond between rod-like particles and the micromechanics of particle-laden interfaces, Soft Matter 8 (2012) 4971–4979, https://doi.org/10.1039/c2sm25211b.

[45] Z. Zhang, P. Pfleiderer, A.B. Schofield, C. Clasen, J. Vermant, Synthesis and directed self-assembly of patterned anisometric polymeric particles, J. Am. Chem. Soc. 133 (2011) 392–395, https://doi.org/10.1021/ja108099r.

[46] L.M. Flores-Tandy, A.V. García-Monjaraz, E.A. van Nierop, E.A. Vázquez-Martínez, J. Ruiz-Garcia, S. Mejía-Rosales, Fractal aggregates formed by ellipsoidal colloidal particles at the air/water interface, Colloids Surf. A Physicochem. Eng. Asp 590 (2020) 124477, https://doi.org/10.1016/j.colsurfa.2020.124477.

[47] S. Coertjens, P. Moldenaers, J. Vermant, L. Isa, Contact angles of microellipsoids at fluid interfaces, Langmuir 30 (2014) 4289–4300, https://doi.org/10.1021/la500888u.

[48] S. Coertjens, R. De Dier, P. Moldenaers, L. Isa, J. Vermant, Adsorption of ellipsoidal particles at liquid-liquid interfaces, Langmuir 33 (2017) 2689–2697, https://doi.org/10.1021/acs.langmuir.6b03534.

[49] M.G. Basavaraj, G.G. Fuller, J. Fransaer, J. Vermant, Packing, flipping, and buckling transitions in compressed monolayers of ellipsoidal latex particles, Langmuir 22 (2006) 6605–6612, https://doi.org/10.1021/la060465o.

[50] B. Madivala, J. Fransaer, J. Vermant, Self-assembly and rheology of ellipsoidal particles at interfaces, Langmuir 25 (2009) 2718–2728, https://doi.org/10.1021/la803554u.

[51] K. Honda, Y. Sazuka, K. Iizuka, S. Matsui, T. Uchihashi, T. Kureha, M. Shibayama, T. Watanabe, D. Suzuki, Hydrogel microellipsoids that form robust string-like assemblies at the air/water interface, Angew. Chem. 131 (2019) 7372–7376, https://doi.org/10.1002/ange.201901611.

[52] A.C. Nickel, T. Kratzenberg, S. Bochenek, M.M. Schmidt, A.A. Rudov, A. Falkenstein, I.I. Potemkin, J.J. Crassous, W. Richtering, Anisotropic microgels show their soft side, Langmuir 38 (2022) 5063–5080, https://doi.org/10.1021/acs.langmuir.1c01748.

[53] Z. Saliternik, The macroscopic differentiation of anopheline eggs according to their pattern on the surface of water, Bull. Entomol. Res. 33 (1942) 221.

[54] D. Benke, T. Feller, M. Krüsmann, A.M. Neuhöfer, F. Ganster, M. Karg, M. Retsch, Prolate spheroidal polystyrene nanoparticles: matrix assisted synthesis, interface properties, and scattering analysis, Soft Matter 19 (2023) 9006–9016.

[55] C.C. Ho, A. Keller, J.A. Odell, R.H. Ottewill, Preparation of monodisperse ellipsoidal polystyrene particles, Colloid Polym. Sci. 271 (1993) 469–479, https://doi.org/10.1007/BF00657391.

[56] M. Rey, J. Walter, J. Harrer, C.M. Perez, S. Chiera, S. Nair, M. Ickler, A. Fuchs, M. Michaud, M.J. Uttinger, A.B. Schofield, J.H.J. Thijssen, M. Distaso, W. Peukert, N. Vogel, Versatile strategy for homogeneous drying patterns of dispersed particles, Nat. Commun. 13 (2022) 1–11, https://doi.org/10.1038/s41467-022-30497-z.

[57] P.J. Yunker, T. Still, M.A. Lohr, A.G. Yodh, Suppression of the coffee-ring effect by shape-dependent capillary interactions, Nature 476 (2011) 308–311, https://doi.org/10.1038/nature10344.

[58] R.S. Jardine, P. Bartlett, Synthesis of non-aqueous fluorescent hard-sphere polymer colloids, Colloids Surf. A Physicochem. Eng. Asp 211 (2002) 127–132, https://doi.org/10.1016/S0927-7757(02)00258-3.

[59] K.A. Brakke, The surface evolver, Exp. Math. 1 (1992) 141–165, https://doi.org/10.1080/10586458.1992.10504253.

[60] B. Midtvedt, S. Helgadottir, A. Argun, J. Pineda, D. Midtvedt, G. Volpe, Quantitative digital microscopy with deep learning, Appl. Phys. Rev. 8 (2021), https://doi.org/10.1063/5.0034891.

[61] Giovanni Volpe, Benjamin Midtvedt, Jesús Pineda, Henrik Klein Moberg, Harshith Bachimanchi, Joana B. Pereira, Carlo Manzo, Deep Learning Crash Course, No Starch Press, 2024.

[62] B.J. Newton, R. Mohammed, G.B. Davies, L. Botto, D.M.A. Buzza, Capillary interaction and self-assembly of tilted magnetic ellipsoidal particles at liquid interfaces, ACS Omega 3 (2018) 14962–14972, https://doi.org/10.1021/acsomega.8b01818.

[63] B.J. Berne, Philip Pechukas, Gaussian model potentials for molecular interactions, J. Chem. Phys. 56 (1972) 4213–4216, https://doi.org/10.1063/1.1677837.

[64] Z.Z. Fu, S.J. Guo, C.X. Li, K. Wang, Q. Zhang, Q. Fu, Hydrogen-bond-dominated mechanical stretchability in PVA films: from phenomenological to numerical insights, PCCP 24 (2022) 1885–1895, https://doi.org/10.1039/d1cp03893a.

[65] J. Menath, J. Eatson, R. Brilmayer, A. Andrieu-Brunsen, D.M.A. Buzza, N. Vogel, Defined core – shell particles as the key to complex interfacial self-assembly, PNAS 118 (2021) 1–10, https://doi.org/10.1073/pnas.2113394118.

[66] M. Rey, A.D. Law, D.M.A. Buzza, N. Vogel, Anisotropic self-assembly from isotropic colloidal building blocks, J. Am. Chem. Soc. 139 (2017) 17464–17473, https://doi.org/10.1021/jacs.7b08503.

[67] E.P. Lewandowski, M. Cavallaro, L. Botto, J.C. Bernate, V. Garbin, K.J. Stebe, Orientation and self-assembly of cylindrical particles by anisotropic capillary interactions, Langmuir 26 (2010) 15142–15154, https://doi.org/10.1021/la1012632.

[68] G. Campos-Villalobos, M. Dijkstra, A. Patti, Nonconventional phases of colloidal nanorods with a soft corona, Phys. Rev. Lett. 126 (2021), https://doi.org/10.1103/PhysRevLett.126.158001.

[69] D. Urban, N. Marcucci, C.H. Wölfle, J. Torgersen, D.R. Hjelme, E. Descrovi, Polarization-driven reversible actuation in a photo-responsive polymer composite, Nat. Commun. 14 (2023), https://doi.org/10.1038/s41467-023-42590-y.